

Jianfeng Xu

Center for Magnetic Recording Research,
University of California,
San Diego 9500 Gilman Drive,
La Jolla, CA 92093
e-mail: john@talkelab.ucsd.edu

Izhak Etsion

Fellow ASME
Department of Mechanical Engineering,
Technion,
Haifa 32000, Israel
e-mail: etsion@technion.ac.il

Frank E. Talke

Fellow ASME
Center for Magnetic Recording Research,
University of California,
San Diego 9500 Gilman Drive,
Mail Code 0401, La Jolla, CA 92093
e-mail: ftalke@ucsd.edu

Failure of Brittle and Ductile Hard Disks Due to High Shock Levels

The failure due to accidental drop of magnetic recording disks made of brittle or ductile materials is of great interest in the design of small form factor hard disk drives. In this study, fracture of glass disks (brittle material) and plastic deformation of aluminum disks (ductile material) at very high shock levels caused by accidental drop are investigated using finite element analysis. It is found that failure inception for both disk types occurs at the inside perimeter of the disk. For glass disks, cracks are found to propagate toward the outer perimeter of the disk along distinct radial lines associated with the largest bending moment of the disk. The critical shock level at which failure originates increases with an increase in the clamp diameter, a reduction in the disk diameter, and an increase in the thickness of the disk. Some experimental results are presented to validate the numerical model. [DOI: 10.1115/1.4000238]

Keywords: shock, ductile, brittle, hard disk drive, magnetic recording

1 Introduction

Disk drives are presently used in many consumer applications such as hand held music players and personal digital assistants. Further application of disk drive technology in cars and other mobile devices are anticipated. Hard disks that are used in mobile devices may experience very high shock levels, on the order of thousands of Gs, if they are dropped accidentally. Many field returns of disk drives, such as those used in ipods, for example, show disk breakage caused by accidental dropping. To guarantee the reliable performance of hard disk drives under those conditions, the characteristics and response of hard disks to high shock levels has become an important design consideration.

A number of studies have been undertaken in the past concerning the dynamic response of hard disk drives due to shock loads. Schreck [1] studied the problem of shock on the head-disk interface experimentally and used the magnetic read back signal to evaluate the damage. Allen and Bogy [2] carried out both experimental work and finite element analysis to determine the effect of shock loads on hard disk substrates, suspensions, and sliders. Edwards [3] performed a finite element analysis of a hard disk drive to study the transient response of the head-disk interface as a function of nonoperational shock loads. Lee et al. [4] studied the transient response of a suspension subject to a shock impulse. Lin [5] investigated the effects of drive enclosure stiffness, disk thickness, actuator stiffness, and bearing stiffness for a 3.5 in. (89 mm) hard disk drive under shock level below 100 G. Zeng and Bogy [6] studied the shock response of a hard disk drive in terms of disk-suspension-slider air bearing systems. Jayson et al. [7] studied numerically the effect of shock on the head-disk interface using a simplified air bearing model to simulate operational conditions. More recently, Murthy et al. [8] investigated the shock response for 3.5 in. (89 mm) and 2.5 in. (63.5 mm) form factor hard disk drives and compared numerical results with experimental results. Feliss et al. [9] studied operational and nonoperational shock for microdrives. They used a scanning laser Doppler vibrometer (LDV) to determine the amplitude and frequency of vibrations of the disk enclosure and investigated whether these vibra-

tions contribute to failure of the head-disk interface. Bhargava and Bogy [10] studied operational-shock response for small form factor hard disk drives numerically. They used commercially available finite element software programs for the suspension and the disk, and a transient air bearing simulation code to study the response of the disk drive to external shocks.

Failure of materials due to shock or impact has also been investigated for situations other than hard disk drives. Bless et al. [11] observed shock waves propagating in a glass rod under dynamic compression. A series of plate impact experiments, bar impact experiments, and impact recovery experiments were performed on brittle materials under various impact conditions by Rosenberg et al. [12–14]. A comprehensive model for failure of brittle materials was discussed by Grady [15]. The model incorporates time-dependent fracture and rate-dependent plasticity. Govindjee et al. [16] introduced a constitutive model for the tensile failure of plain concrete and implemented this model using finite element analysis. Other numerical models were also developed for simulating stresses induced by impact [17].

Failure of ductile materials typically consists of the nucleation, growth, and coalescence of voids [18,19]. Failure modes are affected by the state of stress, plastic strain, pressure, strain rate, and temperature. A set of dynamic experiments for the failure of ductile materials has been discussed by Costin et al. [20]. They used a dynamically loaded, circumferentially notched round bar to study material properties at extremely high loading rates. Many experimental models were developed to simulate the material response under dynamic loading [21,22]. A thorough review has been provided by Rosakis and Ravichandran [23], and Voyiadjis et al. [24]. Such models, along with advanced computational tools, were used for vehicle impact and crash modeling [25,26].

Although many studies have been performed on the shock response of hard disk drives, and on the general topic of failure of materials, none of these studies considered material failure of disks for small form factor hard disk drives due to high shock load. To fill this gap, this paper investigates the fracture and plastic deformation of brittle or ductile magnetic recording disks, respectively, due to shock load using finite element analysis. We consider shock for the nonoperational state when the slider is resting on the disk or when the slider is unloaded from the disk. We are using the so-called “radial return plasticity approach” of Belytschko et al. [27] to numerically simulate the plastic hardening effect in ductile materials. Different failure criteria are pro-

Contributed by the Mechanisms and Robotics Committee of ASME for publication in the JOURNAL OF MECHANICAL DESIGN. Manuscript received March 20, 2009; final manuscript received August 28, 2009; published online October 13, 2009. Assoc. Editor: Panos Y. Papalambros.

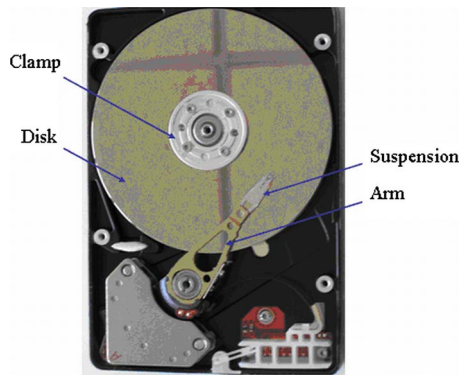


Fig. 1 The structure of a state-of-the-art hard disk drive

posed for crack formation in glass disks and the onset of plastic deformation of aluminum disks due to high shock levels. The results provide design guidelines for the maximum allowable shock levels for disk drives with glass or aluminum disks.

A drop test was performed to validate the accuracy of our finite element model in terms of the disk response to dynamic shock.

2 Definition of the Problem

The structure of a state-of-the-art hard disk drive is shown in Fig. 1. Each disk drive contains a number of magnetic disks, mounted on a spindle motor. The suspension/arm is positioned on the side of the disk and is driven by a voice coil motor. The slider with an integrated thin film read/write element is attached to the backside of the suspension.

To simulate a shock event, a physical model with all the major components of a hard disk drive must first be developed. Then, material properties and boundary conditions need to be defined. Finally, the response of the disk drive to a shock load is determined.

3 Theoretical Background

3.1 Brittle Versus Ductile Material. Brittle and ductile materials are typically classified by their behavior during mechanical testing. One of the most notable differences between brittle and ductile materials is their stress-strain relationship (Fig. 2).

As shown in Fig. 2, brittle materials can sustain only a very small amount of strain before failure. In general, failure occurs suddenly and without much warning. On the other hand, ductile materials can sustain a much larger amount of strain. Furthermore, they can experience strain hardening before failure.

Glass and aluminum are typical examples for brittle and ductile materials, respectively. The material properties of glass and alu-

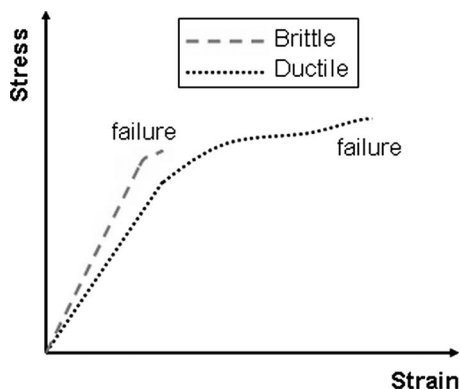


Fig. 2 Typical stress-strain curves for brittle and ductile materials

Table 1 Key material properties

Property	Glass	Aluminum
Young's modulus (GPa)	85	72
Density (kg/m ³)	2.5×10^3	2.7×10^3
Poisson's ratio	0.25	0.33
Yield strength (MPa)	150	200
Fracture toughness (MPa m ^{1/2})	0.7	25
Hardness (GPa)	5.5	0.9
Damping ratio	0.009	0.01

minum used in hard disk drives are shown in Table 1.

As indicated in the table, disks made of glass have higher Young's modulus and higher hardness, but lower yield strength, fracture toughness, and Poisson's ratio as compared with disks made of aluminum. In this paper, we will use glass and aluminum for disks made of brittle and ductile material, respectively.

3.2 Failure Criteria and Strain Hardening. Brittle materials cannot withstand large strains before fracture occurs. In our simulation, a critical plastic strain of 5.0×10^{-6} was selected as the failure criterion for failure inception of glass disks. This value has been used previously in similar investigations reported in the literature [28]. From Table 1 we can see that the yield strain for glass is $\sigma_y/E = 1.76 \times 10^{-3}$ and hence, the critical plastic strain of 5.0×10^{-6} is a very small fraction, about 0.3%, of the yield strain. The maximum tensile strain failure criterion was used in our work for the glass disks. The effects of the magnetic overcoat and of residual stresses on the failure of the glass disks were neglected.

For the aluminum disk we used the data provided in Ref. [28] for strain hardening and assumed linear strain hardening with a tangent modulus of 1%. The von Mises failure criterion was selected to indicate failure inception of the aluminum disk.

4 Model of Disk Drive and Numerical Implementation

The numerical model developed for the disk drive consists of the circular disk, the head gimbal assembly, the disk enclosure, and two clamps (see Fig. 3). The disk simulated in our model is stationary and thus no centrifugal force is considered.

The model was first created in PRO/E [29] and then imported into HYPERMESH, a commercially available pre- and postprocessor for finite element analysis [30]. The model includes mesh, boundary conditions, contact surfaces, and loads. The shock load, denoted by R in Fig. 3, is applied through the two rails of the disk enclosure. The disk was meshed with 602 shell elements that were approximated by parabolic shape function while the disk enclosure was meshed using 2486 solid elements. The disk and disk enclosure are connected by clamps, shaft, and a motor base. A schematic side view of the model is shown in Fig. 4. The clamps are meshed using 634 solid elements. The effect of the shaft and the motor base is simplified by using constrained spot-weld elements.

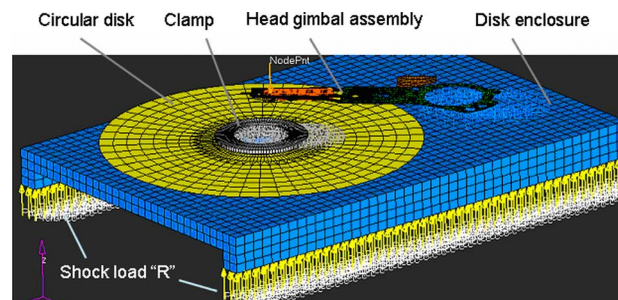


Fig. 3 Finite element model of a disk drive

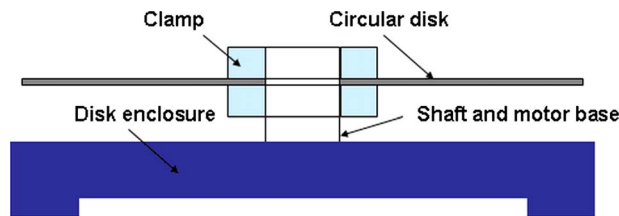


Fig. 4 Schematic side view of the model

The surface of the clamps is parallel to the disk and the clamping force is distributed evenly along the clamp (see Fig. 5). The head/gimbal assembly (see Fig. 3) is modeled using 3219 shell elements and 96 solid elements. The assembly is connected at one end to the disk enclosure through rigid elements. The slider can be positioned over the disk and contact the disk. Contact surfaces are defined between the clamp and the disk, and between the slider and the disk. A value of 0.25 was used for the coefficient of friction of the clamp-disk interface. The clamping force used is 20 N and the slider force (see Fig. 6) when the slider is resting on the disk is 25 mN. These values represent typical values used in current disk drives.

A shock load applied to the two rails of the disk enclosure is modeled by an acceleration profile consisting of a half-sine wave with duration of 1 ms. Throughout this paper, the peak amplitude of the acceleration profile was used to identify the shock level. Figure 7 presents the shock loads for five different shock levels ranging from 1000 G to 5000 G. Disk failure can occur at any point during a shock. When failure first occurs at a certain shock level this level is defined as the “critical shock level.” Commercially available finite element software, LS-DYNA [31], was used to simulate the effect of a given shock load on the disk and to find the critical shock level for the range of shock loads up to 5000 G presented in Fig. 7. During the process of finding the “critical shock level,” we start with an arbitrary shock level and calculate the tensile strains over the entire disk surface throughout the acceleration cycle for time steps of 0.01 ms. If no failure is detected we increase the shock level in steps of 100 G until first failure can

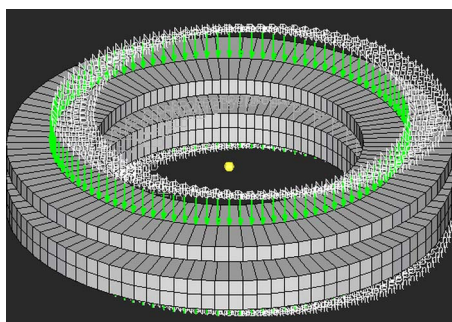


Fig. 5 Finite element model of the disk clamp

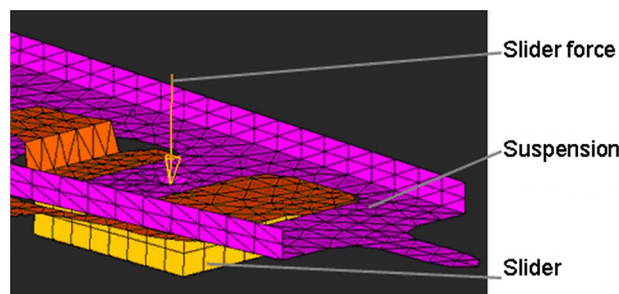


Fig. 6 Point force applied by the slider on the disk

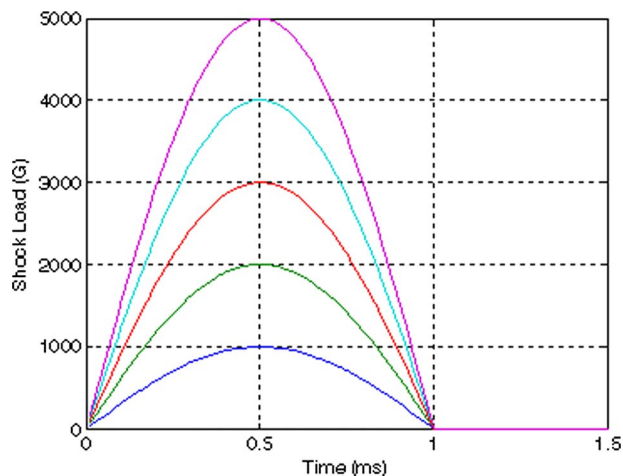


Fig. 7 Shock load versus time as applied to the two rails of the disk enclosure

be observed within a time interval of ± 0.05 ms about the 0.5 ms time corresponding to the peak amplitude of the acceleration profile. In case this first failure occurs below the peak amplitude, outside the ± 0.05 ms time interval, the acceleration value at this instant is selected as the shock level for the next trial.

A number of cases were investigated numerically for shock levels higher than the critical one. This was done to study propagation of cracks in glass disks and plastic strain evolution in aluminum disks, beyond their failure inception.

For glass disks a critical strain of 5.0×10^{-6} was selected as the failure criterion. Cracks start where the strain exceeds this level. The calculated plastic tensile strain is compared with the value of the critical plastic strain at each time step. If the plastic tensile strain of any element reaches the critical plastic strain, this element is deleted, and crack propagation is initiated. As the shock evolves in time the plastic strain of additional elements exceeds the critical value. These elements are also deleted and the crack propagates. It should be noted here that crack propagation can also be modeled based on fracture mechanics.

For aluminum disks, plastic hardening based on the radial return plasticity approach by Belytschko et al. [27] is considered after the maximum von Mises stress reaches the yield strength. This model is able to deal with any type of hardening and is therefore suitable for general plastic behavior in finite element analyses. The numerical implementation for the radial return approach is described in detail in Ref. [32]. Basically, the model presents the relation between stress and strain in the plastic regime by a piecewise linear approximation. It should be noted here that other less sophisticated plasticity laws could also be used.

The radial return plasticity procedure consists of the following steps:

- At each time step the plastic strain increment $\Delta \epsilon^P$ is calculated using

$$\Delta \epsilon^P = \frac{s^* - \sigma_y^n}{3G + E^P} \quad (1)$$

where s^* is an effective trial stress, defined by $s^* = (1.5s_{ij}^{*n+1}s_{ij}^{*n+1})^{1/2}$. Here s_{ij}^{*n+1} is the trial stress at the yield surface for time step $n+1$, σ_y^n is the yield strength at time step n , G is the shear modulus, and E^P is the step-wise linear tangent modulus in the plastic regime.

- The plastic strain ϵ_{n+1}^P is updated for time step $n+1$ using

$$\epsilon_{n+1}^P = \epsilon_n^P + \Delta \epsilon^P \quad (2)$$

- The yield strength σ_y^{n+1} is calculated for time step $n+1$ by

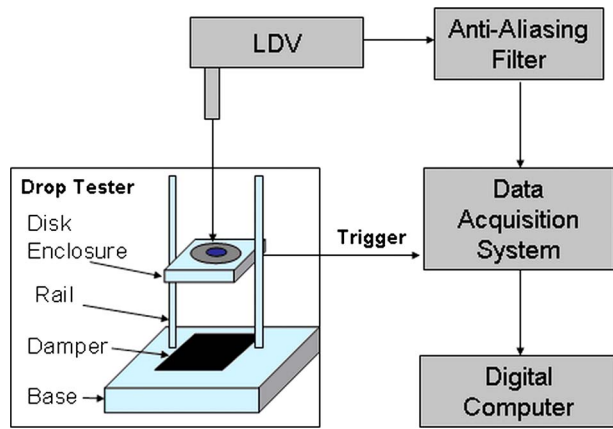


Fig. 8 A schematic of the experimental setup

$$\sigma_y^{n+1} = \sigma_y^n + E^P \Delta \epsilon^P \quad (3)$$

- (d) The scale factor m , using the yield strength at time step $n+1$, is computed as

$$m = \frac{\sigma_y^{n+1}}{s^*} \quad (4)$$

- (e) Finally, the deviatoric stress s_{ij}^{n+1} for time step $n+1$ is returned to the yield surface as

$$s_{ij}^{n+1} = m s_{ij}^{*n+1} \quad (5)$$

5 Drop Test Results and Model Verification

In order to validate the finite element model described in Sec. 4 a special experimental drop test setup was built and used in our laboratory. The experimental setup, as shown schematically in Fig. 8, consists of a drop tester, a LDV, a high pass filter, a data acquisition system, and a digital computer. The drop tester consists of a disk enclosure (without the head gimbal assembly), guide rails, and a base plate with a damper on its top surface. In a drop test, a disk is clamped to the disk enclosure, which is lifted up to a certain height from where it is released and dropped to hit the base plate. The laser beam from the LDV can be aimed either at the disk or the disk enclosure. As soon as the disk enclosure with the clamped disk is released the data acquisition system is triggered and starts capturing the filtered signal from the LDV. The captured signal is transmitted to a digital computer for analysis.

For the validation of the numerical model, we used standard glass disks with 27.4 mm diameter. First, a glass disk was clamped to the disk enclosure and dropped from a fixed height of about 1 m. The acceleration of the disk enclosure was obtained by differentiating the velocity obtained from the LDV. A typical acceleration profile of the top surface of the disk enclosure is plotted in Fig. 9. The dynamics of the acceleration shown in Fig. 9 is typical to drop impact tests [33]. As can be seen the shock load differs from the ideal sine wave shock load shown in Fig. 7. The peak shock amplitude was about 1000 G, followed by small oscillations (positive shock load represents upward acceleration). The same test was repeated with the laser beam aimed at the outer diameter of the disk. The displacement (obtained by integrating the time-dependent velocity measured by the LDV) at the disk outer diameter, during the shock load shown in Fig. 9, is plotted in Fig. 10(a). As can be observed, the maximum peak to peak amplitude of the disk displacement was $36 \mu\text{m}$ and decreased as time evolves.

The shock load shown in Fig. 9 was used as the input shock load for the numerical model described in Sec. 4 above. A glass disk identical to the one used in the drop test was analyzed. The

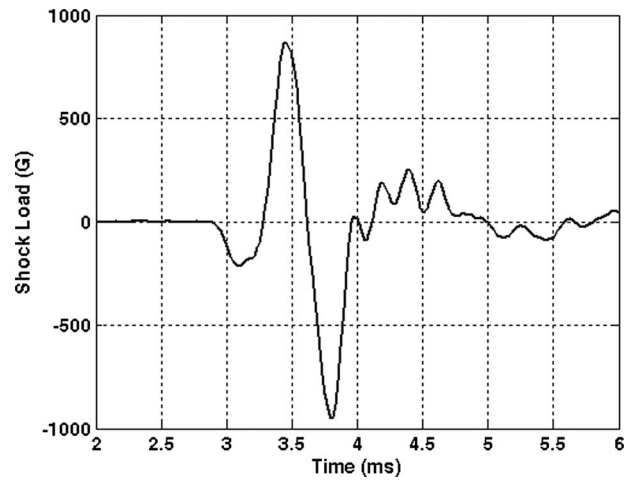


Fig. 9 An experimental drop test acceleration profile of the disk enclosure

calculated displacement at the disk outer diameter is plotted in Fig. 10(b). As indicated in this figure, the theoretical maximum peak to peak amplitude of the disk displacement at its outer diameter is $34 \mu\text{m}$, which is in fair agreement with the experimental results shown in Fig. 10(a). The differences between the experimental and theoretical results can be attributed to different geometries of the experimental disk enclosure, which includes two bearings to allow sliding of the disk enclosure on the guiding rails, and to the presence of a damping pad (see Fig. 8) that is absent in the numerical model. The comparison between experimental and numerical results shown in Fig. 10 verifies the accuracy of the numerical model in a quantitative manner. Interestingly, the peak to peak displacement shown in Fig. 10 is much smaller than the axial clearance (being on the order of $100 \mu\text{m}$ for a 27.4 mm diameter disk) between the disk surface and the surface of the load unload (LUL) ramp used in modern hard disk drives. Hence, although not considered in our analysis, the LUL ramp most likely would not contribute to disk failure by impacting the disk.

6 Crack Formation in Glass Disks and Plastic Deformation in Aluminum Disks

Failure of a glass disk with 27.4 mm diameter in response to a shock level of 4500 G (which is 500 G above the critical shock level found for this case) is shown in Fig. 11 for the case when

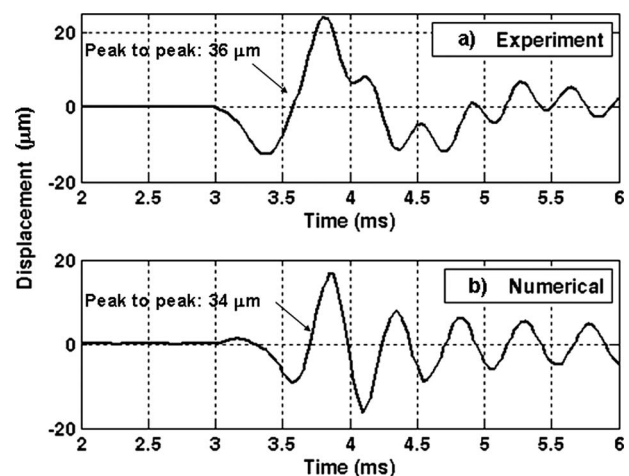


Fig. 10 Displacement of the disk obtained (a) from the drop test experiment and (b) from the numerical model.

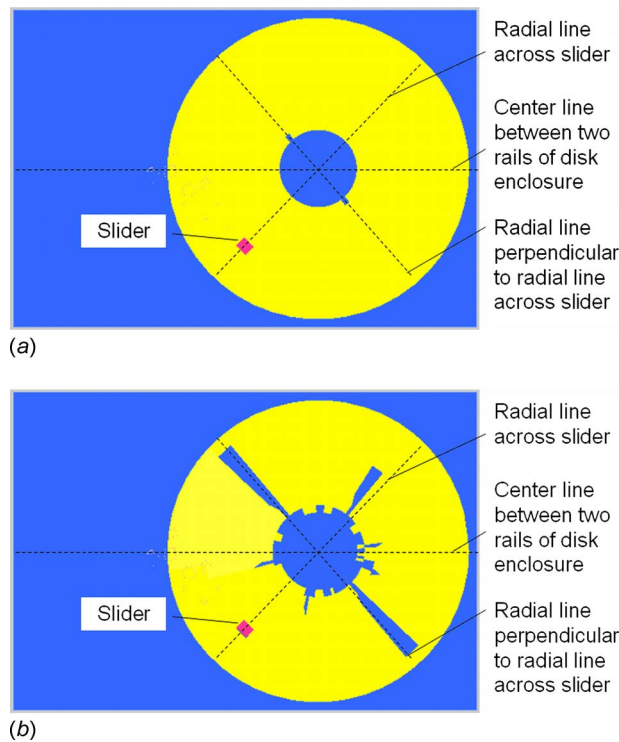


Fig. 11 Failure of a 27.4 mm diameter glass disk in response to a shock level of 4500 G when slider-disk contact is present: (a) failure inception and (b) crack propagation

slider-disk contact is present. This contact is represented by a point force on the disk during the simulation of a shock event (see “slider force” in Fig. 6 and “slider” location in Fig. 11). The failure inception is presented in Fig. 11(a) and crack propagation is shown in Fig. 11(b). Three distinct radial lines are visible in Fig. 11. The first one corresponds to the center line between the two rails of the disk enclosure. This radial line is expected to experience the largest bending moment caused by the shock load R applied to the two rails (see Fig. 3). The second radial line is through the slider-disk contact point, and the third radial line is perpendicular to that through the slider-disk contact point. The third radial line is at the largest possible distance from the slider force point. Hence, this line is expected to experience the largest bending moment caused by the slider force. Indeed as shown in Fig. 11(a), two initial small cracks occur at the inner perimeter of the disk on that third radial line about which the maximum bending moment caused by the slider force was expected. The failure inception occurred approximately 0.36 ms after the start of the shock event (see Fig. 7). As the shock evolves in time the two initial cracks propagate toward the outer diameter of the disk, while additional cracks form and evolve, as shown in Fig. 11(b). The initiation of the first two cracks and their propagation along the radial line of maximum bending moment caused by the slider force suggest that the slider location does affect the crack formation of a glass disk.

To investigate the failure of the same glass disk with 27.4 mm diameter in the absence of slider-disk contact, an identical shock of 4500 G was applied after removal of the slider. In this case, which is shown in Fig. 12, the bending moment of the disk is caused only by the shock load R applied to the two rails (see Fig. 3) and its maximum value is expected about their center line. Indeed, as shown in Fig. 12(a), several cracks initiate at the inner perimeter of the disk (at about 0.37 ms after the start of the shock event), but of all these cracks the two dominant ones are very close to the center line between the two rails. Then, as the shock event progresses, these two dominant cracks expand and propa-

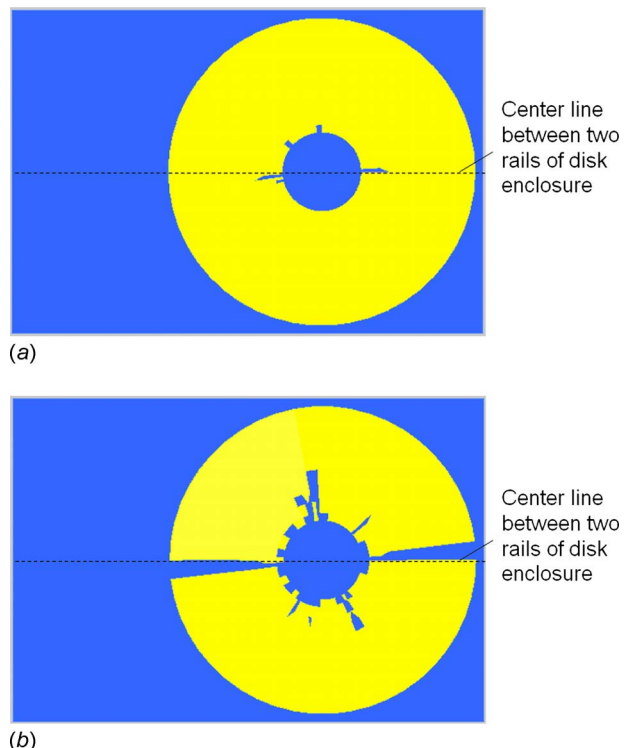


Fig. 12 Failure of a 27.4 mm diameter glass disk in response to a shock level of 4500 G when slider-disk contact is absent: (a) failure inception and (b) crack propagation

gate toward the outer diameter of the disk along the center line of the rails of the disk enclosure, as shown in Fig. 12(b).

Similar failure location to that shown in Fig. 11(a) was observed for an aluminum disk of 27.4 mm diameter in response to a shock of 4500 G (900 G above the critical shock level found for this case) and in the presence of the slider-disk contact. An effective plastic strain of 2.25×10^{-4} appeared on the radial line about which the maximum bending moment caused by the slider force was expected. Then, as the shock event progresses in time, this plastic strain increased and finally reached its maximum value of about 1.28×10^{-3} (at 0.52 ms after the start of the shock). That maximum plastic strain remained on the radial line perpendicular to that through the slider, suggesting that, like the case of the glass disk, the slider position does affect the failure location on the aluminum disk.

The experimental drop test setup described in Sec. 5 was used to qualitatively observe the disk failure. A standard 27.4 mm diameter glass disk was dropped from a height of about 1.2 m and hit the bare base plate (without the damping pad). The glass disk broke into several pieces (>4) with irregular shapes. Although we could not capture exactly the instance of disk breakage due to lack of a high speed camera, the final results of the broken glass disk verified the numerical model in a qualitative manner.

7 Design Factors Affecting the Failure of Glass and Aluminum Disks

The failure inception of glass and aluminum disks is affected by a number of design parameters such as disk thickness, disk diameter, and clamping conditions. In the following, the effect of these parameters on the critical shock level will be presented. The critical shock levels are normalized by 4000 G, which was found as the critical shock level for the standard 27.4 mm glass disk design.

7.1 Disk Thickness. In Fig. 13, the dependence of the critical shock level on the normalized disk thickness is shown, keeping

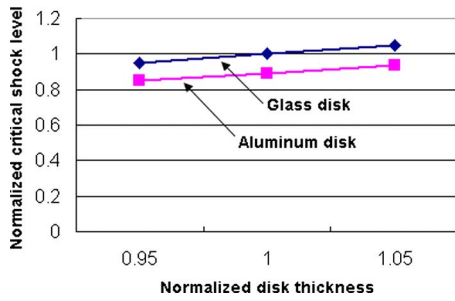


Fig. 13 Critical shock level versus disk thickness (other design parameters are kept constant)

the other entire design parameters constant (clamp outer diameter, clamping force, and disk diameter). The disk thickness is normalized by the “standard” value of 0.381 mm corresponding to the 27.4 mm disk. From Fig. 13, we observe that the critical shock level for failure inception in both glass and aluminum disks increases with disk thickness. Unfortunately, thicker disks, which resist shock failure better, are undesirable since increased disk thickness increases the stack-height of the disk drive.

7.2 Clamping Conditions. The effect of clamping force on the failure inception of glass and aluminum disks is shown in Fig. 14. The clamping force is normalized with a standard value of 20 N. We observe that the fracture inception in a glass disk is insensitive to the clamping force. However, for aluminum disks, we observe a slight decrease in the critical shock level with an increase in the clamping force.

The effect of the outer diameter of the clamp on the failure inception in glass and aluminum disks is shown in Fig. 15. The outer diameter of the clamp is normalized with a standard value of 7.62 mm. We observe that the critical shock level for both glass and aluminum disks increases with an increase in the nondimensional outer diameter of the clamp, i.e., the diameter of the clamp has a strong effect on the critical shock level.

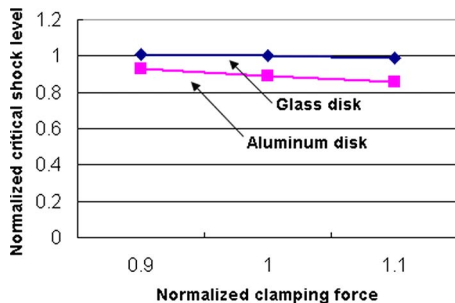


Fig. 14 Critical shock level versus clamping force (other design parameters are kept constant)

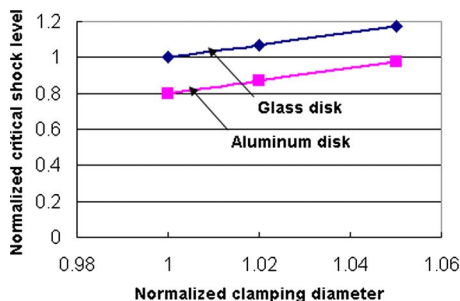


Fig. 15 Critical shock level versus clamp outer diameter (other design parameters are kept constant)

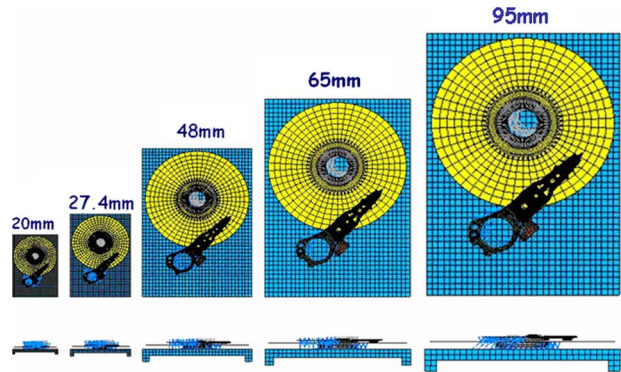


Fig. 16 Finite element models for hard disk drives with different form factors

7.3 Disk Form Factor. Since it is impractical to change the disk diameter alone, without simultaneous structural changes in the entire disk drive system, we will use the form factor rather than the disk diameter as another design parameter. To investigate the effect of the form factor on failure inception, we have repeated the previous simulations for a series of form factors (Fig. 16). In these simulations we have scaled all geometrical parameters by the same ratio (the form factor). In addition, the clamping force was scaled by the same ratio as the form factor. To leave the flying characteristics unchanged, the load applied by the head gimbal assembly on the slider was kept constant at 25 mN.

The dependence of the critical shock level on the normalized form factor at failure inception of glass and aluminum disks is shown in Fig. 17. The disk form factor is normalized with the form factor of the 27.4 mm disk. Clearly, the form factor has the most significant effect on the maximum permissible shock level. The critical shock level increases sharply with a decrease in the disk form factor for both glass and aluminum disks, i.e., the smaller the disk form factor the higher is its resistance to failure. This would be expected because of the smaller bending moments produced by either the rails of the enclosure or the slider point force.

8 Discussion

From the simulation results shown in Sec. 7, we observe that the critical shock level increases when the disk thickness or the outer diameter of the clamp increases or when the disk form factor (and thereby the disk diameter) decreases. To explain these results, we examined a somewhat similar case of “bending of a flat circular plate” (see Fig. 18). The outer edge of the plate is free but its inner edge is clamped [34]. Here, the inner radius b of the plate represents the outer radius of our disk clamp. The outer radius a and the thickness t of the plate represent our disk outer radius and thickness, respectively. A load per unit area q is applied to the plate.

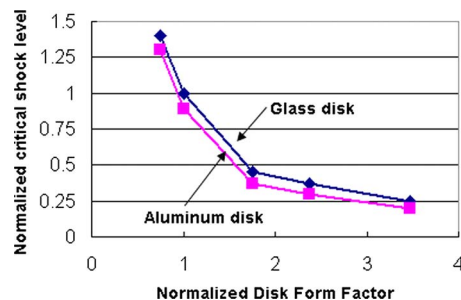


Fig. 17 Critical shock level versus disk form factor

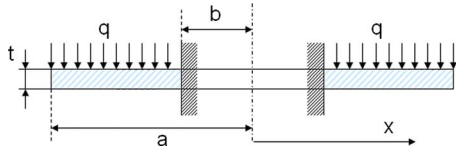


Fig. 18 Bending of a flat circular plate (outer edge free, inner edge clamped) [31]

The maximum bending moment per unit length at the clamped inner circumference of the disk, at radial location b , is given in Ref. [34] by

$$M_{rb} = \frac{qa^2}{C_8} \left[\frac{C_9}{2ab} (a^2 - b^2) - L_{17} \right] \quad (6)$$

The parameters C_8 , C_9 , and L_{17} in Eq. (6) are general functions that are also given in Ref. [34] and can be expressed at $x=b$ by

$$C_8 = \frac{1}{2} \left[1 + \nu + (1 - \nu) \left(\frac{b}{a} \right)^2 \right] \quad (7a)$$

$$C_9 = \frac{b}{a} \left\{ \frac{1 + \nu}{2} \ln \frac{a}{b} + \frac{1 - \nu}{4} \left[1 - \left(\frac{b}{a} \right)^2 \right] \right\} \quad (7b)$$

$$L_{17} = \frac{1}{4} \left\{ 1 - \frac{1 - \nu}{4} \left[1 - \left(\frac{b}{a} \right)^4 \right] - \left(\frac{b}{a} \right)^2 \left[1 + (1 + \nu) \ln \frac{a}{b} \right] \right\} \quad (7c)$$

where ν is the Poisson's ratio. Equation (7) can be rewritten as

$$M_{rb} = qa^2 \left[\frac{C_9}{C_8} \frac{a}{2b} \left(1 - \left(\frac{b}{a} \right)^2 \right) - \frac{L_{17}}{C_8} \right] \quad (8)$$

Equation (8) can be simplified by noting that typical values of the ratio of the inner to outer diameter of hard disk drives give $b/a \approx 0.2$. Hence, higher orders of the ratio b/a can be neglected in Eqs. (7a)–(7c) compared with 1. Thus, C_9/C_8 and L_{17}/C_8 can be approximated as

$$\frac{C_9}{C_8} \approx \frac{\frac{b}{a} \left(\frac{1 + \nu}{2} \ln \frac{a}{b} + \frac{1 - \nu}{4} \right)}{\frac{1}{2} (1 + \nu)} = \frac{2b}{a} \left(\frac{1}{2} \ln \frac{a}{b} + \frac{1 - \nu}{4(1 + \nu)} \right) \quad (9a)$$

$$\frac{L_{17}}{C_8} \approx \frac{\frac{1}{4} \left(1 - \frac{1 - \nu}{4} \right)}{\frac{1}{2} (1 + \nu)} = \frac{3 + \nu}{8(1 + \nu)} \quad (9b)$$

Inserting Eqs. (9a) and (9b) into Eq. (8), the maximum bending moment per unit length at the inner circumference of a disk is approximated as

$$\begin{aligned} M_{rb} &\approx qa^2 \left[\left(\frac{1}{2} \ln \frac{a}{b} + \frac{1 - \nu}{4(1 + \nu)} \right) - \frac{3 + \nu}{8(1 + \nu)} \right] \\ &= qa^2 \left(\frac{1}{2} \ln \frac{a}{b} - \frac{1 + 3\nu}{8(1 + \nu)} \right) \end{aligned} \quad (10)$$

In the absence of any external loading, the load per unit area q is $q = \rho g t$, where ρ is the material density of the disk and g is the constant of gravity. Hence, the maximum bending moment per unit length on this plate due to its own mass is calculated as

$$M_{rb} \approx \rho g t a^2 \left(\frac{1}{2} \ln \frac{a}{b} - \frac{1 + 3\nu}{8(1 + \nu)} \right) \quad (11)$$

The maximum stress caused by the own mass of the plate can be expressed as [34]

$$\sigma_{\max} = M_{rb} \frac{6}{t^2} \approx \frac{6\rho g a^2}{t} \left(\frac{1}{2} \ln \frac{a}{b} - \frac{1 + 3\nu}{8(1 + \nu)} \right) \quad (12)$$

Now, if we increase the acceleration (gravity) to a point where σ_{\max} becomes equal to the yield strength, we can consider this acceleration as being the critical shock level. Hence, considering only the geometrical parameters in Eq. (12), the relationship between the critical shock level and the geometrical parameters can be expressed by

$$G_{\text{crit}} \propto \frac{t}{a^2 \left(\ln \frac{a}{b} - \frac{1 + 3\nu}{4(1 + \nu)} \right)} \quad (13)$$

From Eq. (13), we can see that the critical shock level is linearly proportional to the thickness t in agreement with the prediction in Fig. 13, where a thicker disk can withstand higher shock levels. Similarly, the critical shock level in Eq. (13) is increased when the inner radius b of the plate increases. This trend is in agreement with the results shown in Fig. 15, where an increasing clamp diameter results in a higher critical shock level.

From Eq. (13) we can see that keeping a/b and t/a constant, the critical shock level is inversely proportional to the outer radius a . This correlates with the results shown in Fig. 17.

Increasing the clamp outer diameter reduces the available recording area, while increasing the disk thickness increases the stack height. Both effects are undesirable in the design of disk drives and therefore a compromise is required among all those parameters.

9 Conclusion

The failure mechanism of small form factor hard disks due to high shock levels caused by accidental drop was investigated. It was found that failure inception, in both brittle and ductile material disks, occurs at the inside perimeter of the disk on a radial line about which the bending moment is maximum. When the slider rests on the disk this radial line is perpendicular to that across the slider, otherwise, this radial line is the center line of the two rails.

The effect of several design parameters on the critical shock level at which failure incepts was investigated. It was found that an increase in the outer diameter of the clamp and an increase in the disk thickness cause an increase in the critical shock level. The critical shock level is affected strongly by the disk form factor and sharply increases when the disk becomes smaller. The numerical results were compared with a simplified analytical model for static bending of a flat circular plate and were found in good qualitative agreement.

Disk drive makers are seeking more recordable area in a disk, in addition to stacking more disks into drives so as to increase capacity for each drive. This study indicates that a design compromise is needed between increase in drive capacity and critical shock level in terms of clamp diameter and disk thickness.

References

- [1] Schreck, E., 1994, "Magnetic-Readback-Mapping and its Application to the Slider/Disk Interface Damage Due to Shock Impact," *STLE Proceedings on Tribology and Mechanics of Magnetic Storage Systems Symposia, IX*, pp. 5–10.
- [2] Allen, A. M., and Bogy, D. B., 1996, "Effects of Shock on the Head Disk Interface," *IEEE Trans. Magn.*, **32**, pp. 3717–3719.
- [3] Edwards, J. R., 1999, "Finite Element Analysis of the Shock Response and Head Slap Behavior of a Hard Disk Drive," *IEEE Trans. Magn.*, **35**, pp. 863–867.
- [4] Lee, S. J., Hong, S. K., and Lee, J. M., 2001, "A Study of Shock-Resistance Design of Suspension Subjected to Impulsive Excitation," *IEEE Trans. Magn.*, **37**, pp. 826–830.
- [5] Lin, C. C., 2002, "Finite Element Analysis of a Computer Hard Disk Drive Under Shock," *ASME J. Mech. Des.*, **124**, pp. 121–125.
- [6] Zeng, Q. H., and Bogy, D. B., 2002, "Numerical Simulation of Shock Response of Disk-Suspension-Slider Air Bearing Systems in Hard Disk Drives," *Microsyst. Technol.*, **8**, pp. 289–296.
- [7] Jayson, E. M., Murthy, J., Smith, P. W., and Talke, F. E., 2002, "Shock and Head Slap Simulations of Operational and Nonoperational Hard Disk Drives,"

- IEEE Trans. Magn., **38**, pp. 2150–2152.
- [8] Murthy, A. N., Feliss, B., Gillis, D., and Talke, F. E., 2006, “Experimental and Numerical Investigation of Shock Response in $3\frac{1}{2}$ and $2\frac{1}{2}$ Inch Form Factor Hard Disk Drives,” *Microsyst. Technol.*, **12**, pp. 1109–1116.
- [9] Feliss, B., Murthy, A. N., and Talke, F. E., 2007, “Microdrive Operational and Non-Operational Shock and Vibration Testing,” *Microsyst. Technol.*, **13**, pp. 1015–1021.
- [10] Bhargava, P., and Bogy, D. B., 2007, “Numerical Simulation of Operational-Shock in Small Form Factor Hard Disk Drives,” *ASME J. Tribol.*, **129**, pp. 153–160.
- [11] Bless, S. J., Brar, N. S., Kanel, G., and Rosenberg, Z., 1992, “Failure Waves in Glass,” *J. Am. Ceram. Soc.*, **75**, pp. 1002–1004.
- [12] Rosenberg, Z., Bourne, N. K., and Millett, J., 1996, “Direct Measurements of Strain in Shock-Loaded Glass Specimens,” *J. Appl. Phys.*, **79**, pp. 3971–3974.
- [13] Bourne, N. K., Millett, J., Rosenberg, Z., and Murray, N., 1998, “On the Shock Induced Failure of Brittle Solids,” *J. Mech. Phys. Solids*, **46**, pp. 1887–1908.
- [14] Millett, J. C. F., Bourne, N. K., and Rosenberg, Z., 2000, “Direct Measurements of Strain in a Shock-Loaded Lead Filled Glass,” *J. Appl. Phys.*, **87**, pp. 8457–8460.
- [15] Grady, D. E., 1998, “Shock-Wave Compression of Brittle Solids,” *Mech. Mater.*, **29**, pp. 181–203.
- [16] Govindjee, S., Kay, G. J., and Simo, J. C., 1995, “Anisotropic Modeling and Numerical Simulation of Brittle Damage in Concrete,” *Int. J. Numer. Methods Eng.*, **38**, pp. 3611–3633.
- [17] Elías, D. A., and Chiang, L. E., 2003, “Dynamic Analysis of Impact Tools by Using a Method Based on Stress Wave Propagation and Impulse-Momentum Principle,” *ASME J. Mech. Des.*, **125**, pp. 131–142.
- [18] Curran, D. R., Seaman, L., and Shockey, D. A., 1987, “Dynamic Failure of Solids,” *Phys. Rep.*, **147**, pp. 253–388.
- [19] Seaman, L., Curran, D. R., and Shockey, D. A., 1976, “Computational Models for Ductile and Brittle Fracture,” *J. Appl. Phys.*, **47**, pp. 4814–4826.
- [20] Costin, L. S., Duffy, J., and Freund, L. B., 1977, “Fracture Initiation in Metals Under Stress Wave Loading Conditions,” American Society of Testing and Measurement, Paper Nos. STP627-EB and STP27395S.
- [21] Nakamura, T., Shih, C. F., and Freund, L. B., 1985, “Elastic-Plastic Analysis of a Dynamically Loaded Circumferentially Notched Round Bar,” *Eng. Fract. Mech.*, **22**, pp. 437–452.
- [22] Nishioka, T., and Atluri, S. N., 1983, “Path-Independent Integrals, Energy Release Rates, and General Solutions of Near-Tip Fields in Mixed-Mode Dynamic Fracture Mechanics,” *Eng. Fract. Mech.*, **18**, pp. 1–22.
- [23] Rosakis, A. J., and Ravichandran, G., 2000, “Dynamic Failure Mechanics,” *Int. J. Solids Struct.*, **37**, pp. 331–348.
- [24] Voyiadjis, G. Z., Palazotto, A. N., and Gao, X.-L., 2002, “Modeling of Metallic Materials at High Strain Rates With Continuum Damage Mechanics,” *Appl. Mech. Rev.*, **55**, pp. 481–493.
- [25] Ma, D., and Lankarani, H. M., 1997, “A Multibody/Finite Element Analysis Approach for Modeling of Crash Dynamic Responses,” *ASME J. Mech. Des.*, **119**, pp. 382–387.
- [26] Yang, R. J., Wang, N., Tho, C. H., Bobineau, J. P., and Wang, B. P., 2005, “Metamodeling Development for Vehicle Frontal Impact Simulation,” *ASME J. Mech. Des.*, **127**, pp. 1014–1020.
- [27] Belytschko, T., Liu, W. K., and Moran, B., 2000, *Nonlinear Finite Elements for Continua and Structures*, Wiley, New York.
- [28] 2003, *DYNA Models for Crash Simulation of Automobiles*, Insurance Institute for Highway Safety.
- [29] 2004, *PRO/ENGINEER User Manual*, Parametric Technology Corporation, Needham, MA.
- [30] 2002, *HYPERMESH User Manual*, Altair Computing Inc., Troy, MI.
- [31] 2003, *LS-DYNA User Manual*, Livermore Software Technology Corporation, Livermore, CA.
- [32] Hallquist, J. O., 1998, *LS-DYNA Theoretical Manual*, Livermore Software Technology Corporation, Livermore, CA.
- [33] Wong, E. H., 2005, “Dynamics of Board-Level Drop Impact,” *ASME J. Electron. Packag.*, **127**, pp. 200–207.
- [34] Young, W. C., and Budynas, R. G., 2002, *Roark’s Formulas for Stress and Strain*, 7th ed., McGraw-Hill, New York.